Comparison of flow patterns and droplet deformations of modified sharp-edged and conical orifices during high-pressure homogenisation using μPIV

Ariane Bisten[1] · Dominik Rudolf[1] · Heike P. Karbstein[1]

Abstract
Micro-particle image velocimetry was used as an optical, non-intrusive measurement method to measure the flow pattern and visualise droplet deformation in high-pressure homogenisation disruption units of two different inlet designs (sharp-edged and conical). The flow patterns were compared either at same Reynolds numbers ($Re = 980$) or pressure differences ($\Delta p = 52$ bar) each, to describe the influence of inlet geometry on the droplet disruption efficiency. Therefore, the shear and elongation rates were calculated from the velocity profiles and discussed regarding the visualised deformation of the emulsion droplets. For this, the viscosity ratio between the droplet and continuous phase was varied. Afterwards, the droplet size distributions (DSD) of emulsions with corresponding viscosity ratio passing the sharp-edged and the conical orifice were characterised. The inlet geometry influenced the flow pattern, shear and elongation rate profile, droplet deformation and finally droplet size distributions during the high-pressure homogenisation. On the one hand, sharp-edged inlet design resulted in higher axial velocity profiles and smaller droplets with slightly bimodal character. On the other hand, conical inlet design resulted in perfectly monomodal DSD but comparatively bigger droplets.

Graphical abstract
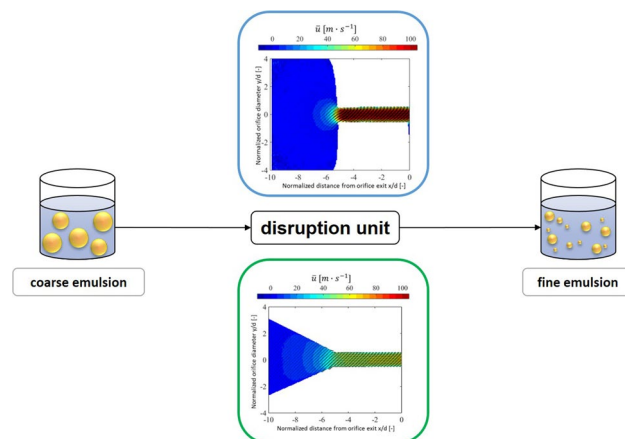
Heike P. Karbstein: formerly: Schuchmann.

Extended author information available on the last page of the article

1 Introduction

Emulsions are widely used products in the pharmaceutical (Davis et al. 1985), chemical (Heusch 1987), cosmetic (Breuer 1985) and food (Walstra 1997) industry. Their properties, such as colour, rheological behaviour and stability, are mostly influenced by the droplet sizes and their distribution (Walstra 1983). High-pressure homogenisation (HPH) is an established process to produce emulsions with droplet size distributions in the lower μm and nm size range (Phipps 1982; Merkel et al. 2015; Heike 2016). In HPH, emulsions premixes or coarse emulsions are pressurised to several 100–1000 bar and relaxed after passing the narrow disruption units, like flat valves or orifices. As a result, the droplet size is dramatically reduced. The flow pattern before, in and after the disruption unit leads to shear, elongation, turbulence and cavitation. These local stresses results in droplet break-up leading to smaller droplets (Phipps 1982; Stang et al. 2001; Tesch and Schubert 2001). Adjusting or changing the droplet size distributions in a HPH process is often based on empirical knowledge, even today (Walstra 1983; Phipps 1982, 1975; Stang et al. 2001; Floury et al. 2000; Köhler and Schuchmann 2015). On the microscale, droplet break-up is strongly influenced by the local flow pattern. Therefore, understanding the local stresses, which lead to droplet break-up, is essential to enable specific adaptations of the HPH processes and targeted product design (Floury et al. 2000; Brösel and Schubert 2001; Kolb et al. 2001; Tesch et al. 2002; Budde et al. 2002; Blonski et al. 2007; Innings and Tragardh 2007; Håkansson et al. 2011; Ball et al. 2012; Kelemen et al. 2014; Bisten and Schuchmann 2016).

One parameter, that influences the local stresses and thus the resulting droplet size distribution (DSD), is the geometry of the disruption unit. As it was shown in previous works, even a slight geometric modification of the disruption unit resulted in different DSD under identical process conditions (Kolb et al. 2001; Aguilar et al. 2008; Ramamurthi and Nandakumar 1999; Wibel 2009). Also it was shown that the elongation rate in front of the orifice depends on the shape of the orifice in a simulation (Håkansson et al. 2012; Steiner et al. 2006; Kissling et al. 2011). Additionally, it was stated that with higher elongation rates the droplet deformation, and therefore the droplet break-up after the orifice, is enhanced. However, due to the complex flow conditions and the microscale of the disruption unit, the results could not be experimentally verified at that time.

One relatively new and very promising approach to determine the local stresses and investigate their influence on droplet deformation and break-up is the optical and non-intrusive measurement method named micro-particle image velocimetry—μPIV (Santiago et al. 1998; Meinhart et al. 1999; Lindken et al. 2009). This measuring method was already successfully applied to investigate the HPH process in modified, optical accessible orifices (Kelemen et al. 2014, 2015; Gothsch et al. 2011, 2014). During μPIV measurements, the fluid is seeded with tracer particles small enough to accurately follow the flow pattern. The entire fluid volume, as well as the tracer particles, are illuminated by pulsed laser light. The seeding particles are fluorescent, absorb the laser light and emit light at a different wavelength. Filters, which allow the emitted light to pass through, help in increasing the signal-to-noise ratio. The analyses of the cross-correlation are calculated from the displacement of the particles between the double images—so-called two-dimensional, two-velocity component (2D2C) measurements (Bisten and Schuchmann 2016; Santiago et al. 1998; Lindken et al. 2009; Adrian and Westerweel 2011; Kähler et al. 2012; Cierpka et al. 2012; Raffel et al. 2007; Koutsiaris et al. 1999; Meinhart et al. 1999; Mielnik and Saetran 2004; Wereley and Meinhart 2010).

In previous investigations, specific microstructured orifices were used, all depicting a sharp-edged inlet geometry (Kelemen et al. 2014, 2015; Gothsch et al. 2014). Modern flat valves used in technical HPH processes, e.g., in dairy or fruit juice processing, have a conical inlet geometry. In this investigation, we designed a modified orifice with conical inlet geometry and compared its flow pattern to the flow pattern found in an orifice with sharp-edged inlet geometry. The determination of the flow pattern enabled the calculation of the elongation and shear rates in front of and in the orifice itself. We then visualised the deformations of single droplets added to the fluid. The viscosity ratio between droplet and continuous fluid was varied as parameter influencing droplet deformation (Walstra 1983; Kelemen et al. 2015). During the experimental part, the Reynolds number or the pressure difference were kept constant to ensure either comparable hydrodynamic conditions or energy density. In the end, the influence of the inlet geometry on the disruption efficiency was discussed on the resulting DSD.

2 Experimental section

2.1 Materials

The continuous phase consisted of demineralised water and 10% w/w polyethylene glycol of molar mass $M = 20.000$ g/mol (PEG 20.000 ROTIPURAN®, Carl Roth, Karlsruhe, Germany) for adjustment of the dynamic viscosity η_c to 13.5 mPa s. The dynamic viscosity η_c was measured with a rotational rheometer (Anton Paar Physica MCR 101, Graz, Austria) at 100 1/s and 20 °C. Newtonian flow behaviour was

detected in the investigated shear rate range of $1 - 1000$ s^{-1}. During the velocity measurements, 1.8 µm fluorescent seeding particles (micro-particles GmbH, Berlin, Germany) were added in a concentration of 0.00125% w/w to ensure the required particle concentration per interrogation volume (Keane and Adrian 1990).

The emulsification experiments were performed with two different medium-chain triglycerides (Miglyol®, Cremer Oleo, Hamburg, Germany) of different viscosities as disperse phase (see Table 1). The surface tension between the disperse and continuous phase, including the additives, was determined in equilibrium state using a Wilhelmy plate (DCAT11, dataphysics, Filderstadt, Germany) to $\gamma \approx 4$ mN/m. The fluorescent dye Nile red (9-(diethyl-amino) benzo[a]phenoxazin-5(5H)-one, Sigma-Aldrich Chemie GmbH, St. Louis, USA) was dissolved in the oil phase. The continuous phase included 0.5% w/w Polysorbate 20 (Tween 20®, Carl Roth, Karlsruhe, Germany) as surfactant for stabilisation against coalescence.

The emulsification process of the coarse emulsion was adjusted to achieve a similar droplet size of $x_{50,3} \approx 68$ µm for different viscosities. Therefore, emulsions were produced either with a propeller stirrer at 200 rpm or with the gear ream dispersing machine Ultra-Turrax® at 5000 rpm with emulsification time of 10 min (see Table 1). The coarse emulsions were diluted with PEG solution to a disperse phase fraction of $\phi = 0.0125\%$ v/w. At such a low concentration coalescence can be neglected (Karbstein 1994; Danner and Schubert 2001) and single droplets can be visualised without overlapping during the experiments. The relevant characteristics/parameters of the coarse emulsions are summarised in Table 1.

2.2 Experimental set-up

The experimental set-up for the flow pattern measurements as well as for the droplet visualisation experiments is shown in Fig. 1. The continuous phase was provided from the pressure vessel (a), which allows a maximum pressure of $p_{max} = 100$ bar. The fluid was pressurised using a nitrogen pressure bottle (b), which enables a pulsation-free flow. Digital pressure indicators (PI) were used to monitor the pressure in front and behind the optical accessible orifice (e), which was mounted on the top of the µPIV system. A valve (g) was used to apply back-pressure p_{bp}. The ratio between the applied back-pressure p_{bp} and the inlet pressure p_{inlet} was set to a Thoma number of $Th = p_{bp}/p_{inlet} \approx 0.3$. It was shown that the optical cavitation was suppressed and the droplet break-up was optimised at this Thoma number (Schlender et al. 2016).

During the experiments, either the same Reynolds number or the same pressure difference were used. The Reynolds number is defined as ratio between inertia and viscous forces (48). The $Re = \frac{d \cdot \bar{u} \cdot \rho_c}{\eta_c}$ was calculated using the hydraulic diameter of the orifice d as characteristic length scale, the average flow velocity of the fluid $\bar{u} = \frac{\dot{V}}{w \cdot h}$ (with $\dot{V}$ as volume flow, and w and h as width and height of the orifice), the density of the fluid ρ_c and the dynamic viscosity of the continuous phase η_c. The pressure difference Δp was defined as the inlet pressure p_{inlet} against the applied back-pressure p_{bp}.

For the visualisation of the droplets, the set-up was slightly modified. Two pipe coils (d, f) were added in front (length of $l = 0.7$ m and diameter of $d = 10$ mm) and behind (length of $l = 2.1$ m and diameter of $d = 2$ cm) the orifice (e). For each experiment, the pipe coil (d) was filled with

Table 1 Parameters and used materials of the coarse emulsion

Continuous phase	Solution	10% w/w PEG 20.000, demineralized water	
	Surfactant	0.5% w/w Tween® 20[a]	
	η_c	13.5 mPa s[b]	
		Emulsion I	Emulsion II
Disperse phase	Oil	Miglyol® 812	Miglyol® 829
	Dye	140 ppm Nile red	140 ppm Nile red
	η_d	31.1 mPa s[b]	251.5 mPa s[b]
	$\lambda = \frac{\eta_d}{\eta_c}$	= 2	= 19
Dispersed phase fraction		0.0125% v/w	0.0125% v/w
Droplet size $x_{50,3}$ of coarse emulsions		≈ 67 µm	≈ 69 µm
Emulsification process		Stirrer, 200 rpm 10 min	Ultra-Turrax® (IKA, Staufen im Breisgau, Germany), 5000 rpm, 10 min
Interfacial tension[c]		≈ 4 mN/m	≈ 4 mN/m

[a]Only added during the emulsification experiments

[b]Measured at 20 °C and a shear rate of 100 1/s

[c]Measured at 20 °C and after $t = 60$ min
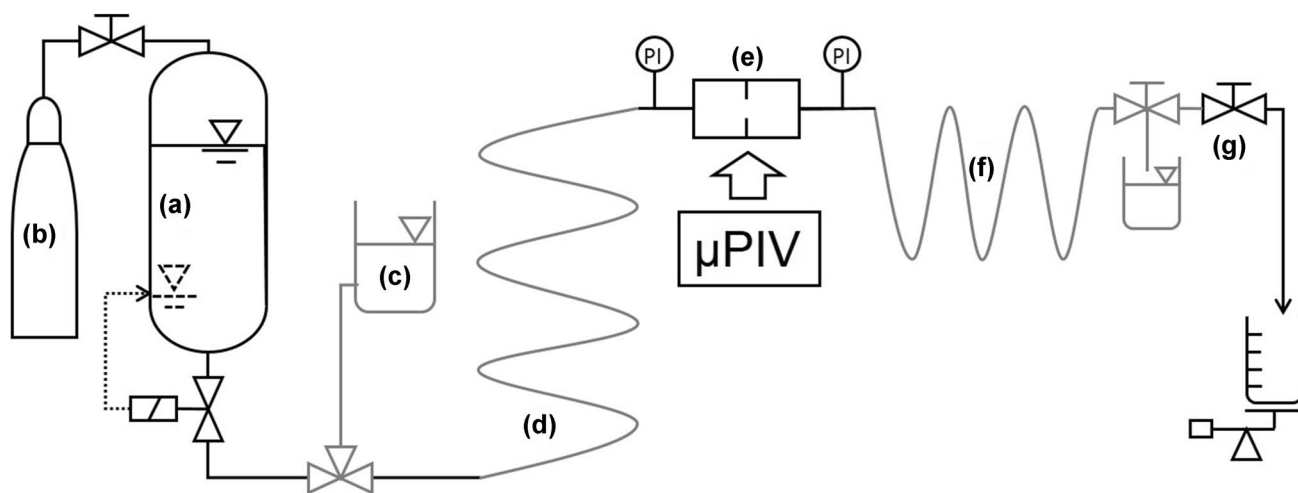
Fig. 1 Experimental set-up with (a) pressure vessel, (b) nitrogen bottle, (c) storage tank for coarse emulsion, (d) pipe coil, (e) optically accessible orifice, (f) pipe coil for sample taking, (g) valve to apply back-pressure

coarse emulsion and then rinsed with continuous phase from the pressure vessel. After a certain time, the experiment was stopped and a sample of the fine emulsion was taken from the pipe coil (f) to prevent further droplet break-up in the valve (g).

Two optically accessible orifices were used during the experimental procedure as shown in Fig. 2. The orifices were constructed of a stainless steel block, where the orifices were milled in, and sealed with an optical-grade PMMA glass plate afterwards. For both orifices, the width and height of the squared orifice was $w = 200$ μm and $h = 200$ μm and a length of $l = 1$ mm. The width and height of the orifices were referred as diameter d later on. The focal plane was in all experiments 100 μm below the PMMA glass plate, at the centreline of the orifices. The orientation of the orifices was always at the top of the steel block to realise an optical
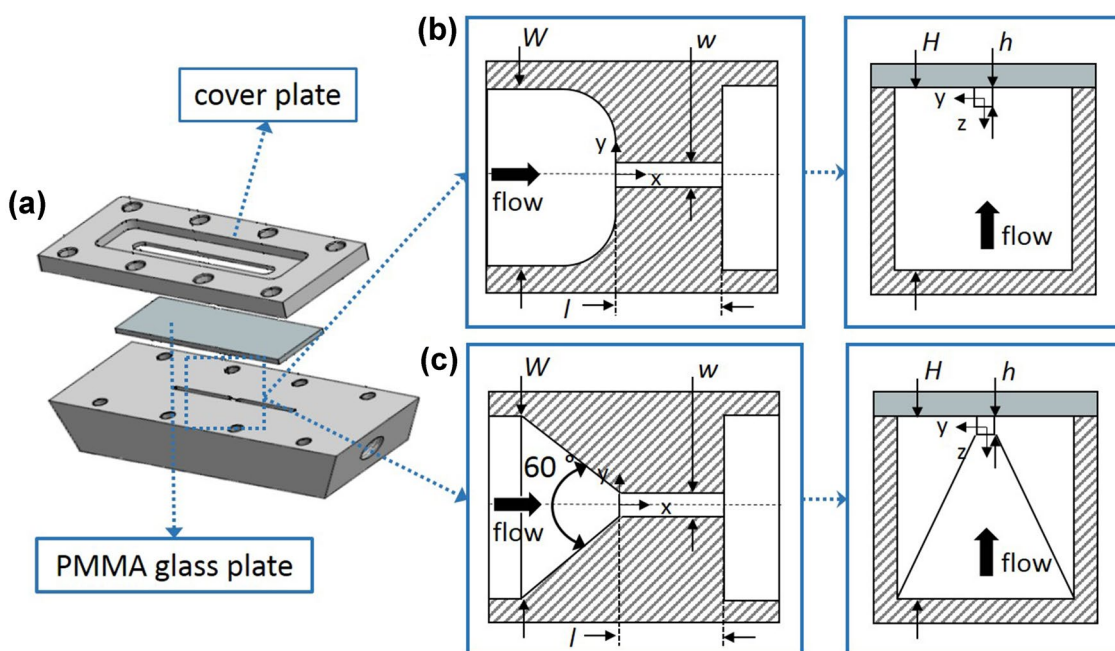
Fig. 2 a Modified orifices with the PMMA glass plate and cover plate; the width of $w = 200$ μm and height of $h = 200$ μm (diameter $d = 200$ μm) of the orifices and the length of $l = 1$ mm, and a width of $W = 2$ mm and a height of $H = 2$ mm for the inlet and outlet of the orifices. **b** Sharp-edged transition from the entrance to the orifice. **c** Conical (pyramidal) transition with an angle of 60°; the flow direction in both orifices is from left to right

access. Orifice A had a sharp-edged transition from the inlet to the orifice, while orifice B had a conical (pyramidal) transition with an angle of 60°. The width and height of the inlets and outlets were $W = 2$ mm and $H = 2$ mm.

In a fully symmetrical orifice, the maximum flow velocity $\dot{u}_{max}$ should be found on the centreline, i.e., 100 μm below the upper or above the lower orifice wall, being our measurement plane. However, the geometries used here were not symmetrical in the inlet region. This was due to the need of optimal optical accessibility. Consequently, only the orifices were perfectly symmetrical (see Fig. 2).

Droplet visualisation experiments were repeated five times, and samples were collected. The resulting droplet size distributions of the collected samples were measured by a laser diffraction particle analyser (HORIBA LA-940, Retsch Technology, Haan, Germany). The samples were measured in a stirred fraction cell. The refractive index for the continuous phase was $1.449 + 0.000i$. An overview of conducted experiments is shown in Table 2.

2.3 μPIV measurements

For the illumination of the images, a double-pulsed ND:YAG laser (Dual Power 30.15 of Litron Lasers, Rugby, Great Britain) was operated at a frequency of 8 Hz and attenuated to 32 mJ/pulse with a wavelength of 532 nm. The time between the double images Δt was set between 0.2 and 1.0 μs depending on the velocity of the fluid. A laser light guide connected the laser beam to an inverse microscope (DM IRM, Leica Microsystems Wetzlar GmbH, Wetzlar, Germany). An objective lens (C PLAN, Leica Microsystems Wetzlar GmbH, Wetzlar, Germany) with a 10× magnification and a numerical aperture of NA = 0.22 was used to generate the focal plane. The double images were recorded by a 2048 × 2048 pixel CCD camera (FlowSense 4M, Dantec Dynamics, Skovlunde, Denmark) with a 12 bit resolution. The imaged region was approximately 3×3 mm with a final magnification of one pixel corresponding to 1.5 μm.

A total number of 747 double images were taken during each experiment, to ensure deviation in stationary velocity smaller than 0.3%. In order to enhance the signal-to-noise ratio and reduce the bias by the depth of correlation (DOC), the images were processed by subtracting a mean image

Table 2 Overview of conducted experiments

Orifices Geometry	Reynolds number Re	Homogenisation pressure Δp
Orifice A (sharp-edged)	≈ 980	≈ 53 bar
Orifice B (conical)	≈ 980	≈ 20 bar
	≈ 1710	≈ 51 bar

and setting an intensity threshold to minimise errors arising from background noise as proposed by Rossi et al. (2012). A multi-pass cross-correlation algorithm from Dynamic Studio 3.4 (Dantec Dynamics, Skovlunde, Denmark) was used to calculate the velocity vectors, considering the shift of the particles in one double image. The interrogation window sizes were decreased from 128×128 pixels to the final resolution of 16×16 pixels to ensure a high resolution at a large velocity range. Thus, a final distance of 11.2 μm between vectors was used. These vectors represented the velocity field for each double image. A mean velocity field was then calculated from the 747 individual double images, not considering erroneous vectors. The shear and elongation stresses were calculated from the mean vector field at the inlet and in the orifice, assuming stationary flow conditions. The shear and elongation gradients between each vector and its neighbour within a 20 μm distance were calculated and averaged over a 5×5 interrogation area. A detailed description of the used analysis methods as well as the shear and elongation stresses were developed and verified at our department, and published in Kelemen et al. (2014, 2015).

The images of the droplet deformation were only analysed if they contained a single, focused droplet. To improve the image quality a mean image was subtracted from all images using the Dynamic Studio 3.4 software. In a second step, the greyscale was inverted and a median filter was applied in Irfanview 4.36 (Wiener Neustadt, Austria). In total, between 1498 and 2996 images for each emulsion were analysed and 60–80 representative images were superimposed for the visualisation.

3 Results and discussion

3.1 Flow velocity fields, shear and elongation rates in the modified orifices

The flow conditions at the entrance of the modified sharp-edged and the conical orifices were compared with each other at a Reynolds number of $Re \approx 980$. At this Reynolds number, the pressure difference was $\Delta p \approx 52$ bar in the sharp-edged orifice and $\Delta p \approx 20$ bar in the conical orifice. In both geometries, the flow fields in front of the orifices were laminar and stationary. As predicted by the Thoma number, no signs of cavitation were detected in the orifices themselves or the outlet.

The mean flow velocity fields of the sharp-edged and the conical orifice inlet regions are presented in Fig. 3. Local flow velocities in the sharp-edged orifice (Fig. 3a) increased abruptly at the entrance of the orifice and remained high and constant at $\bar{u} = 92$ m/s between $x/d \approx 0$ and $x/d \approx 5$, with x being the distance from the orifice inlet in flow direction, and d the orifice height and width, respectively. In the
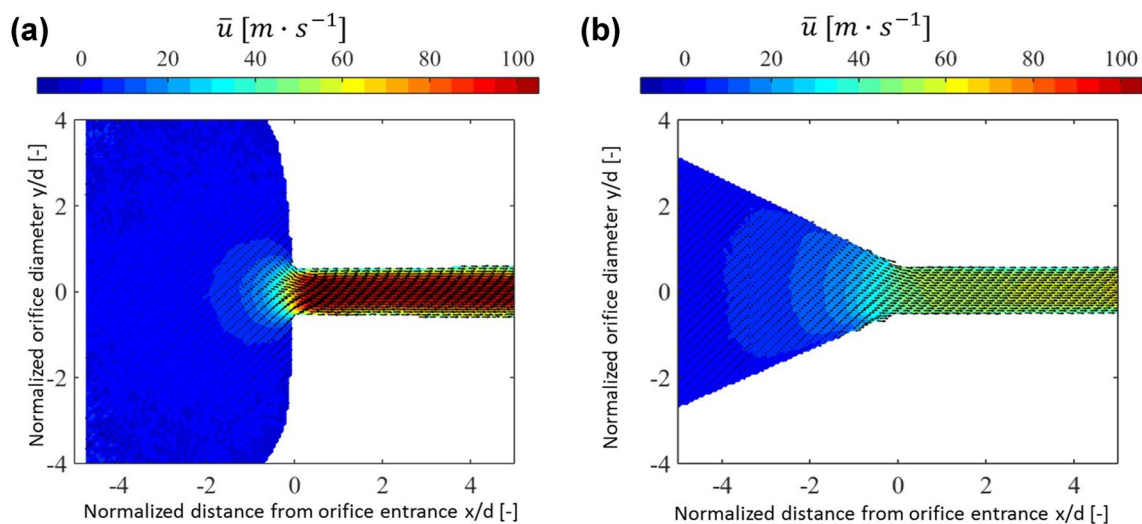
Fig. 3 Mean flow velocity fields $\bar{u}$ in the orifices with **a** sharp-edged and **b** conical inlet at overall Reynolds number of $Re \approx 980$. **a** Pressure difference $\Delta p \approx 52$ bar; **b** pressure difference $\Delta p \approx 20$ bar

near-wall regions, the velocities were always fast decreasing to 0 m/s. The flow profile starting at $x/d \approx 0$ was not exact symmetrical in the centreline: in the upper near-wall region with $y/d > 0$, the velocity profile was slightly different to the opposite near-wall region at $y/d < 0$. We assume, those differences were caused by inaccuracies in the manufacturing process of the orifice. Due to sharp edge at the entrance of the orifice, a detachment of the flow caused by increasing velocity fluctuations was detected. Cavitation bubbles were not observed in the outlet at the experimental conditions (see also Kelemen et. al. 2014, 2015). To ensure no cavitation during the experiments, the Thoma number was set to 0.3. At this number, cavitation in aqueous solutions is very unlikely (Schlender et al. 2016; Gothsch et al. 2016).

Compared to the sharp-edged orifice, local velocities increased slowly in front of the entrance of the conical orifice at $Re \approx 980$ (Fig. 3 b). In general, the measured velocities at the same measurement plane (100 μm below the optical accessible wall) were significantly reduced to those found in the sharp-edged geometry. In the orifice itself, the flow field in the centre of the orifice was uniform and the differences of the velocities in the near-wall regions and centre of the orifice were moderate. The maximum flow velocity, however, was not always at the centreline of the orifice ($\bar{u}_{max} \neq \bar{u}_{centre}$).

Measured velocity fields enabled the calculation of the local shear and elongation rates. The shear rates $\dot{\gamma}$ in the sharp-edged and conical orifice are presented in Fig. 4. In the sharp-edged orifice (Fig. 4a), relevant shear rates were found only in the orifice. They were detected starting at the entrance to the orifice and in the orifice itself, with the highest values in the near-wall region. Different to the sharp-edged orifice, the shear rates in the conical orifice already

increased at the inlet ($-2 < x/d < 0$), close to the orifice. In both regions, inlet and orifice, the highest shear rate values were detected in the near-wall region (Fig. 4b), corresponding to highest flow velocity differences (Fig. 3b). Two main differences caused by different inlet geometries can be summarised so far: (1) sharp-edged inlet geometry caused higher pressure drop at same hydrodynamic conditions ($Re \approx 980$) leading to higher velocities and shear rates in the orifice and (2) conical inlet geometry provided shear rates outside the orifice in the inlet region.

Local elongation rates $\dot{\epsilon}$ in the sharp-edged and the conical orifice are presented in Fig. 5. The main elongation stress occurred at the entrance to the orifice for both geometries. Right before the inlet at $-1 < x/d < 0$, the elongation rate $\dot{\epsilon}$ (Fig. 5a) increased in the sharp-edged entrance due to radial acceleration of the flow. Regarding the maxima of $\dot{\epsilon}$ (edges of the orifice), this can be attributed to the detachment of the flow, also known as vena contracta (51). Shortly after the inlet, the radial acceleration decreased and the elongation rate $\dot{\epsilon}$ diminished rapidly. However, the area of maximum elongation rates ($\dot{\epsilon} > 9 \times 10^5$ s^{-1}) in front of the conical orifice (Fig. 5b) was larger than in front of the sharp-edged orifice ($-2 < x/d < 0$).The main difference in elongation rates was found at the transition from the inlet to the orifice ($x/d = 0$ and $-0.5 < y/d < 0.5$) in both inlet geometries: (1) sharp-edged inlet geometry caused higher elongation rates in the centre trajectory ($\dot{\epsilon} \approx 6 \times 10^5$ s^{-1}) while (2) elongation rates in the conical inlet were significantly smaller ($\dot{\epsilon} \approx 2 \times 10^5$ s^{-1}).

Apparently, different inlet geometries caused differences in Δp at same Reynolds number and therefore same hydrodynamic conditions. We therefore increased the pressure difference to $\Delta p \approx 52$ bar in the conical orifice to operate
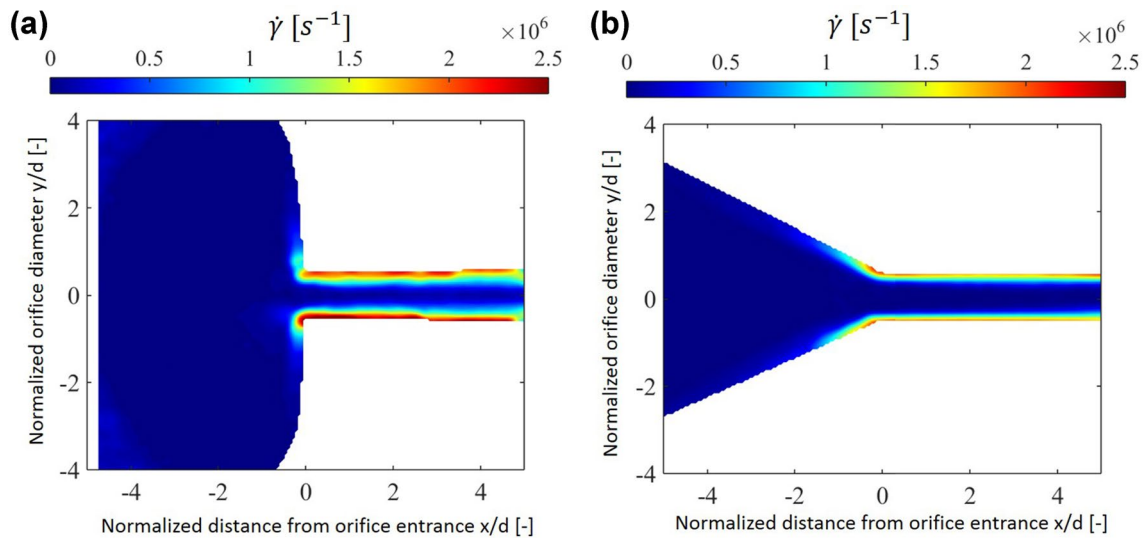
Fig. 4 Calculated shear rates $\dot{\gamma}$ in the orifices with **a** sharp-edged and **b** conical inlet geometry at constant Reynolds number of $Re \approx 980$. **a** Pressure difference $\Delta p \approx 52$ bar; **b** pressure difference $\Delta p \approx 20$ bar
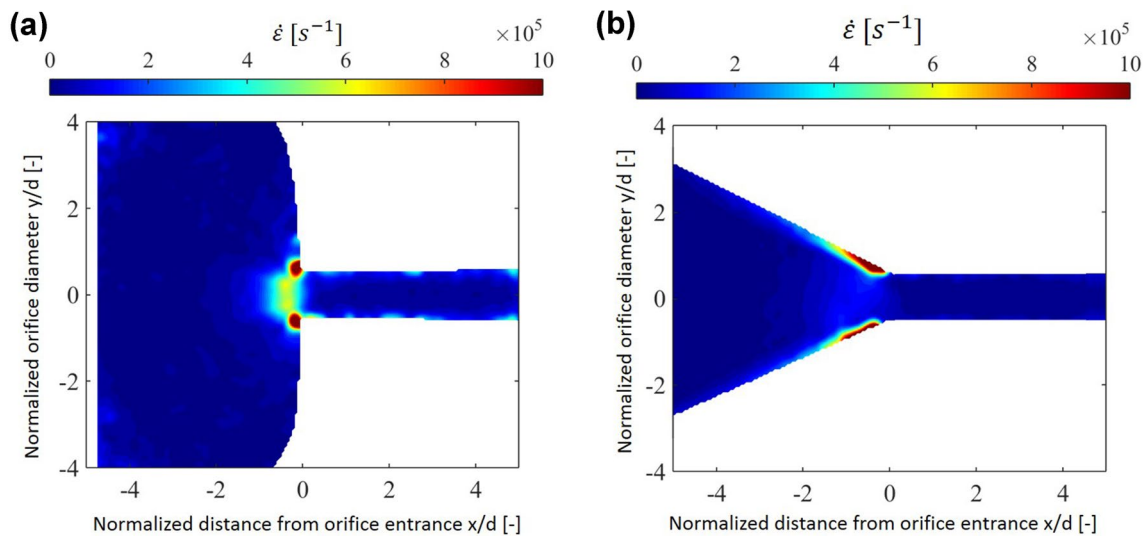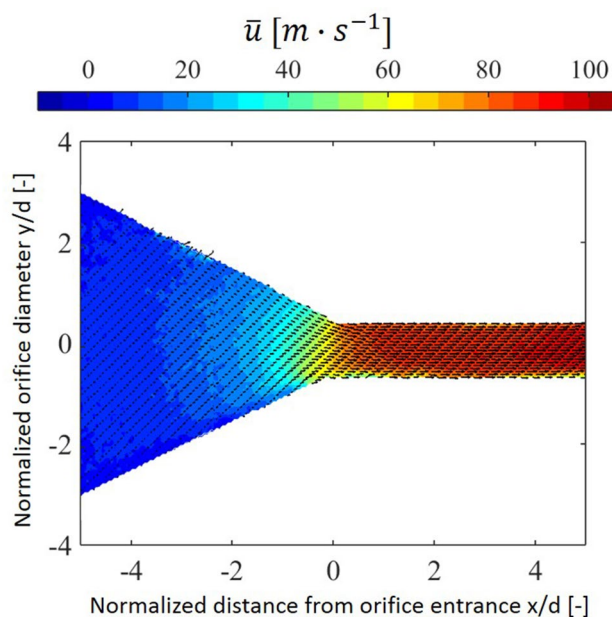

Fig. 5 Calculated elongation rates $\dot{\epsilon}$ for the orifices with **a** sharp-edged and **b** conical inlet at constant Reynolds number of $Re \approx 980$. **a** Pressure difference $\Delta p \approx 52$ bar; **b** pressure difference $\Delta p \approx 20$ bar

at comparable pressure difference Δp as in the sharp-edged orifice at $Re \approx 980$, leading to a Reynolds number of $Re \approx 1710$; see Fig. 6. The flow velocity fields were similar in profile as in the sharp-edged inlet geometry with reduced Reynolds number ($Re \approx 980$). The acceleration of the velocity at the inlet of the conical orifice, however, was smoother as in the sharp-edged inlet; see Fig. 3a. In the orifice, flow velocities were similar in value and distribution. Again, slight asymmetries were detected (compared values measured at $y/d \approx 1$ to those measured at $y/d \approx -1$) according to manufacturing inaccuracies.

The shear rates $\dot{\gamma}$ in the conical orifice at $Re \approx 1710$ were higher compared to the conical orifice at $Re \approx 980$ and even to the sharp-edged orifice at $Re \approx 980$, see Fig. 7, maintaining the characteristic profile found for lower Reynolds number, see Fig. 4 a. Significantly increased shear rate values $\dot{\gamma}$ were also found in the near-wall inlet region of the orifice ($-1.5 < x/d < 0$).

The elongation rates $\dot{\epsilon}$, Fig. 8, had also increased compared to the elongation rates calculated at $Re \approx 980$. Especially in the inlet region ($-4 < x/d < -2$), a more uneven structure was detected with increased values especially in

Fig. 6 Mean flow velocity fields $\bar{u}$ in the orifice with conical inlet at a Reynolds number of $Re \approx 1710$ with a pressure difference of $\Delta p \approx 52$ bar

Fig. 7 Calculated shear rates $\dot{\gamma}$ in the orifice with conical inlet at a Reynolds number of $Re \approx 1710$ with a pressure difference of $\Delta p \approx 52$ bar

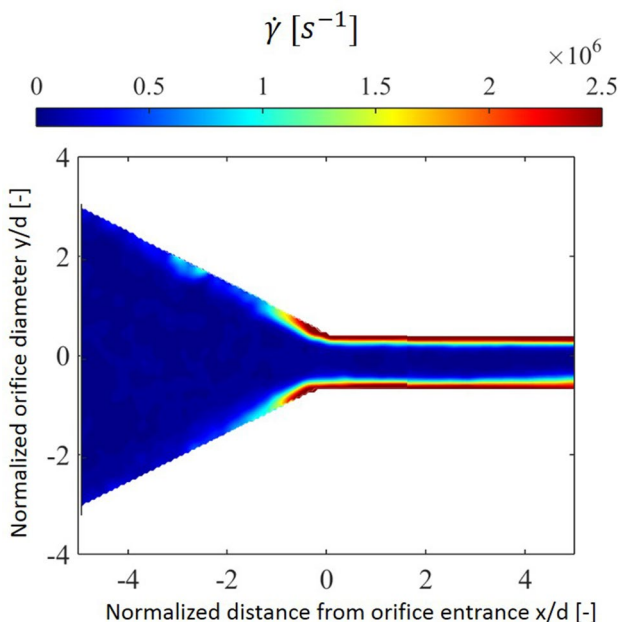the near-wall region ($y/d \approx 2$). In total, higher values were found for the elongation stresses compared to the sharp-edged orifice geometry at same pressure difference, but reduced Reynolds number ($Re \approx 980$). However, it should be mentioned that the spatial resolutions of the µPIV for

Fig. 8 Calculated elongation rate $\dot{\varepsilon}$ for the orifice with conical inlet at a Reynolds number of $Re \approx 1710$ with a pressure difference of $\Delta p \approx 52$ bar

the sharp-edged and the conical orifices was limited due to gradient effects, especially at the near-wall proximities (Kelemen et al. 2015; Kähler et al. 2006, 2012).

3.2 Droplet deformation and break-up

Droplets with different viscosity ratios ($\lambda = 2$ and $\lambda = 19$), but same starting droplet sizes were visualised using similar process conditions as applied in the flow profile investigations. The visualisation of 60–80 representative droplets (from 1498 to 2998 images) in the region $-5 \approx x/d \approx 5$ is depicted in Fig. 9 for a Reynolds number of $Re \approx 980$ and $Re \approx 1710$.

For both viscosity ratios, the inlet geometry and resulting stress distributions clearly influence the deformation of the droplets in the flow field. At high viscosity ratio of $\lambda = 19$, these differences resulting from the inlet geometry were more pronounced, since high viscosity ratios tend to hinder droplet deformation (Walstra 1983; Plateau 1873; Taylor 1934; Rumscheidt and Mason 1961; Grace 1982; Bentley and Leal 1986; Stone et al. 1986; Stone 1994). Especially the start of the deformation was influenced by viscosity ratio: while deformation started at large distance to orifice at $-5 < x/d$ at $\lambda = 2$, it only started late at $-1 < x/d$ at $\lambda = 19$ ($Re \approx 980$), and at $-2.5 < x/d$ at $\lambda = 19$ ($Re \approx 1710$), respectively.

Passing the orifice with the sharp-edged inlet, droplets at $\lambda = 2$ were highly deformed and elongated to thin filaments at $Re \approx 980$, in some cases even before the droplets
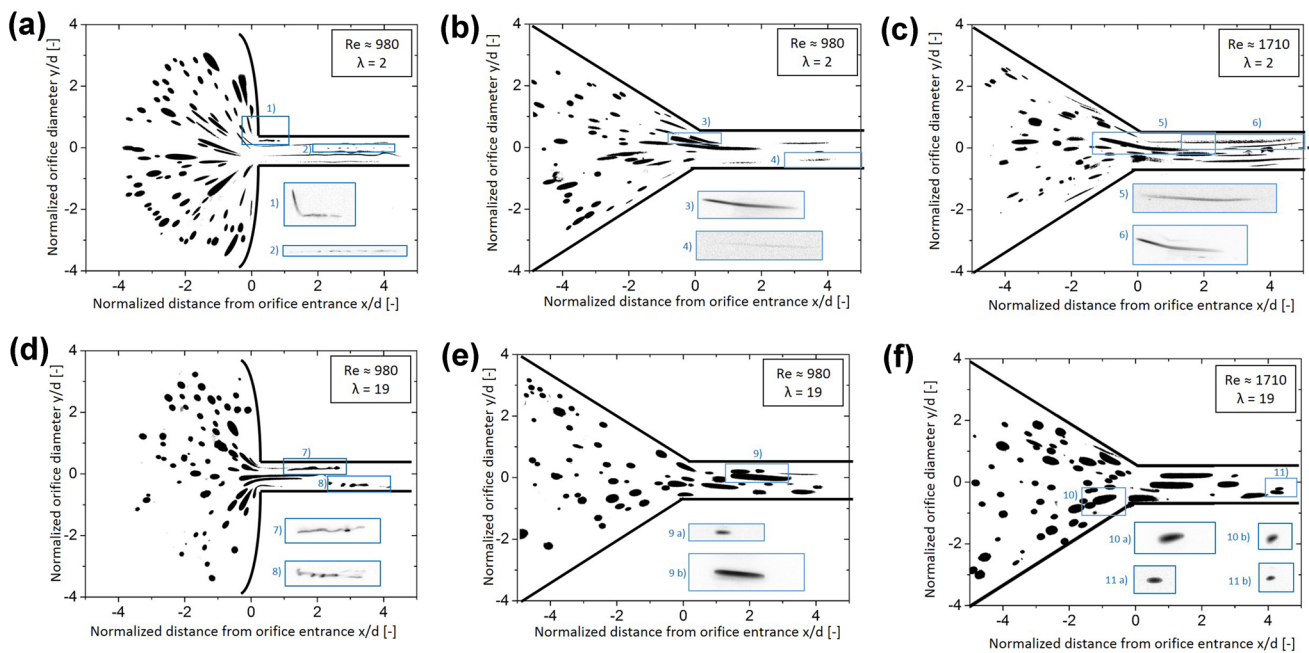
Fig. 9 Deformed droplets at the inlet of the orifices. Sharp-edged (**a, d**) and conical inlet (**b, e**) at $Re \approx 980$ and conical inlet at $Re \approx 1710$ (**c, f**). Emulsions with a viscosity ratio of **a–c** $\lambda = 2$ and **d–f** $\lambda = 19$. **a, c, d, f** Pressure difference of $\Delta p \approx 52$ bar and (**b, e**) $\Delta p \approx 20$ bar

entered the orifice. In comparison, droplets passing the orifice with the conical inlet at $Re \approx 980$ were less deformed and elongated to thicker and shorter filaments. Increasing the pressure difference to a Reynolds number of $Re \approx 1710$ increased the deformation and elongation of the droplets, but still led to thicker filaments than passing the orifice with the sharp-edged inlet at $Re \approx 980$.

Increasing the viscosity ratio to $\lambda = 19$, droplets passing the orifice with the sharp-edged inlet started to deform significantly later, and formed filaments of higher thickness. This was even more pronounced in the orifice with conical inlet, even at increased Reynolds numbers: at $Re \approx 980$, nearly no deformation occurred in front of the orifice and in the orifice itself, filaments were thicker than those formed at $\lambda = 2$. At $Re \approx 1710$, the droplet deformation increased in front of the inlet; however, in the orifice itself the filaments were similarly deformed as at $Re \approx 980$.

Filaments formed in the sharp-edged orifice inlet were not only thinner, but also curlier in the orifice itself, leading to lower contrasts in the images.
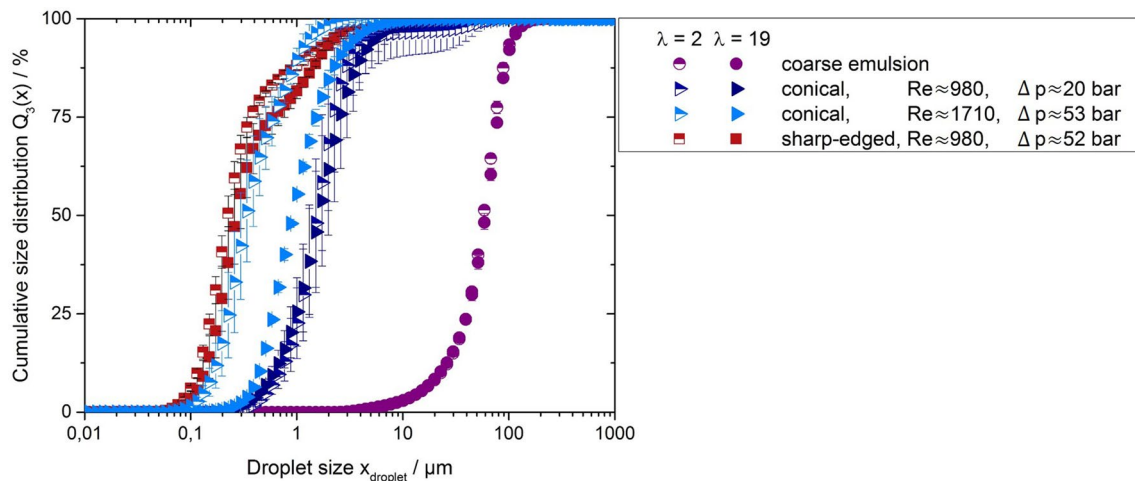
3.3 Droplet size distribution

The resulting droplet size distributions are shown in Fig. 10. The droplet size distribution (DSD) of the coarse emulsions was set to $x_{50,3} \approx 68$ μm (shown in violet) to ensure the same starting conditions for all experiments independent of the viscosity ratio.

The inlet geometry clearly had an influence on resulting droplet size distribution either at constant Reynolds numbers or pressure difference. The sharp-edged inlet region—showing the strongest droplet deformation to thinnest filaments (see Fig. 9)—resulted in smallest droplets after break-up. At constant Reynold numbers ($Re \approx 980$), DSD had significantly reduced mode values of $x_{50,3} \approx 225$ nm for the sharp-edged inlet, and $x_{50,3} \approx 900$ nm for the conical one.

Comparing emulsions of different viscosity ratios ($\lambda = 2$ and $\lambda = 19$), different effects were detected: the sharp-edged inlet resulted in DSD with comparable mode ($x_{50,3} \approx 225$ nm for $\lambda = 2$ and $x_{50,3} \approx 265$ nm for $\lambda = 19$). However, a higher number of bigger droplets ($x > 300$ nm) were found for $\lambda = 19$. The appearance of bigger droplets in the sharp-edged orifice was connected to the droplet break-up efficiency and/or coalescence processes behind the orifice (can not be resolved with our set-up). This effect was less significant for the conical inlet at the same $Re \approx 980$. In general, the best force transition into droplet break-up were expected at viscosity ratios near one. Therefore, we measured more efficient droplet break-up with smaller modal values in same geometries and at same hydrodynamic conditions at $\lambda = 2$, than at $\lambda = 19$.

After the increase of the Reynolds number to $Re \approx 1710$ in the orifice with the conical inlet, in order to obtain the same pressure difference of $\Delta p \approx 52$ bar as in the orifice with the sharp-edged inlet, the DSD for emulsions of $\lambda = 2$ showed a comparable mode to the mode which was formed in the orifice with sharp-edged inlet ($x_{50,3} \approx 225$ nm for the

Fig. 10 Droplet size distributions of the coarse emulsions, as well as of the fine emulsions after passing the orifices with sharp-edged and conical inlet geometry. Viscosity ratio of $\lambda = 2$ and $\lambda = 19$, Reynolds number ≈ 980, corresponds to a pressure difference of $\Delta p \approx 52$ bar for the sharp-edged and $\Delta p \approx 20$ bar for the conical orifice, and $Re \approx 1710$ with a pressure difference of $\Delta p \approx 53$ bar for the conical orifice

sharp-edged inlet and $x_{50,3} \approx 330$ nm for the conical). However, the bigger droplet fraction ($x > 300$ nm) found for the sharp-edged inlet disappeared using the orifice with conical inlet geometry leading to nearly monomodal DSD. Using the same conical inlet geometry at high viscosity ratio of $\lambda = 19$, the resulted DSD was significantly larger than at $\lambda = 2$, but was smaller than at $Re \approx 980$. On the one hand, the DSD was not affected by the viscosity ratio in the conical inlet geometry at low Reynolds number. On the other hand, the difference between the DSDs at different viscosity ratios at high Reynolds number was immense. Since the droplet deformations according to Fig. 9 were similar at low and high Reynolds numbers for $\lambda = 19$ the cause of different DSDs must originate at events taking place behind the orifice. Expansion of our set-up for observation of emulsification behind the orifice are a subject of our ingoing work and will be presented in our subsequent publications.

In summary, the DSDs of droplets produced in orifice with sharp-edged inlet geometry at same Reynolds numbers or pressure difference were always smaller, than droplets produced in orifices with conical inlet. Sharp-edged inlet geometry resulted in larger energy dissipation at same hydrodynamic conditions, and resulted in stronger droplet deformation and only little viscosity ratio dependency.

4 Conclusions

High-pressure homogenisation is usually applied when droplets of small sizes (diameter < 1 μm) are required. Usually, the pressure difference is given as the main droplet size influencing parameter, but some also prefer the Reynolds

number for the experiments. However, it is also reported that the orifice geometry has an influence on resulting pressure difference.

Therefore, we constructed two high-pressure disruption units with same dimensions of the orifice, but different inlet geometry: while the inlet was sharp-edged in one of the orifices, the other orifice was build with a pyramidal transition (angle 60°), here named "conical inlet".

Local flow velocities, shear rates $\dot{\gamma}$ and elongation rates $\dot{\epsilon}$ were calculated. The velocity profiles showed a clear influence of the orifice inlet geometry on the shear and elongation rate values and distributions affecting the droplet deformation at same Reynolds numbers or pressure difference each.

Different inlet geometries resulted in different velocity profiles: while the orifice with sharp-edged inlet showed a sudden acceleration of the flow velocity in front of the orifice and maximum velocities up to 100 m/s in the centre of the orifice, the acceleration in front of the conical orifice was smoother with lower velocities up to 60 m/s in the centre of the orifice at same Reynoldsnumber. Increasing the pressure difference of the conical orifice to $\Delta p \approx 52$ bar and $Re \approx 1710$ led to similar velocity profiles in the near-wall region as in the sharp-edged orifice. However, the acceleration in front of the conical orifice remained smoother.

Different velocity profiles resulted in different shear and elongation rates in the orifices with sharp-edged and conical inlet geometries. At $Re \approx 980$, the highest shear rate values occurred in the orifice with sharp-edged inlet, in the near-wall regions of the orifice, while the shear rate values in the orifice with conical inlet at $Re \approx 980$ and $Re \approx 1710$ were higher in front of the orifice. At comparable pressure difference ($\Delta p \approx 52$ bar), the orifice with conical inlet showed

also higher shear rates in the near-wall region of the orifice as the orifice with the sharp-edged inlet. The sharp-edged orifice, however, had higher velocity gradients between the centre of the orifice and the wall. The elongation rate values in the orifice with sharp-edged inlet increased sharply in front of the orifice and diminished rapidly in the orifice. The region of effective elongation (area with high elongation rates) increased in the orifice with conical inlet and was larger in front of the orifice than in the orifice itself.

Emulsions were produced in both geometries, either at the same Reynolds number or at the same pressure difference. Two viscosity ratios were chosen, one in the region of elongation and shear-dependent deformation ($\lambda = 2$), the other one in the region with mostly elongation-dependent deformation ($\lambda = 19$).

Independent of the Reynolds number and the viscosity ratio, the geometry of the orifice inlet influenced the deformation of the droplets and elongation of the filaments. The sharp-edged inlet resulted in earlier and stronger deformation of the droplets in front of and in the orifice. Within the orifice droplets always formed filaments, being thinner than in the conical orifice, especially when shear-induced deformation was more difficult due to higher viscosity ratio ($\lambda = 19$). Increasing the pressure difference in the orifice with conical inlet did not increase the deformation to the level of the deformation in the sharp-edged orifice inlet, leading to thicker filaments.

Three general differences in resulting DSD were connected to the different geometries of the disruption unites, causing different velocity profiles, shear and elongation rates and thus different droplet deformation: HPH using (1) the orifice with sharp-edged inlet resulted in smallest droplets but non-monomodal distribution; (2) while monomodal DSDs were accomplished in the orifice with conical inlet; (3) the viscosity dependency of droplet break-up was negligibly small when the orifice with the sharp-edged inlet was used, while serious differences were found for the orifice with conical inlet at increasing pressure difference. Here, droplets of $\lambda = 2$ were broken to significantly smaller sizes compared to droplets of $\lambda = 19$.

This work clearly shows the impact of the orifice inlet geometry on resulting velocity profiles, shear and elongation rate values and their distribution on droplet deformation, which in turn influences the droplet break-up and the resulting droplet size distribution. With the current set-up, only the velocity, elongation, shear and elongation profiles were optically accessible using the µPIV technique. Decay of the deformed filaments in smaller droplets, however, was only accessible in an offline droplet size measurement after the homogenisation processes. Therefore, direct observation of the droplet break-up after the orifices are the next step to gain mechanistic understanding of high-pressure homogenisation processes. Thus, the expansion of our µPIV set-up for observations of the droplet break-up after the orifices is a subject of our ongoing work and will be presented in our subsequent papers.

Author contributions HPK had the principal idea for this approach; the experimental approach was first tested by KK, AB and HPK; AB and HPK conceived and designed the experiments for this paper; AB and DR performed the experiments; AB analysed the data; DS and HL from the Institute for Micro Process Engineering (Micro Apparatus Engineering—FAB) contributed to the micro manufacturing of the orifices; AB and HPK discussed and analysed the results; AB and HPK wrote the paper.

Compliance with ethical standards

Conflict of interest The authors declare no conflict of interest. The founding sponsors had no role in the design of the study, analyses, or interpretation of data; in the writing of the manuscript, and in the decision to publish the results.

References

Adrian RJ, Westerweel J (2011) Particle image velocimetry. Cambridge University Press, Cambridge

Aguilar F, Köhler K, Schubert H, Schuchmann HP (2008) Herstellen von Emulsionen in einfachen und modifizierten Lochblenden: Einfluss der Geometrie auf die Effizienz der Zerkleinerung und Folgen für die Maßstabsvergrößerung. Chem Ing Tec 80(5):607–613

Ball CG, Fellouah H, Pollard A (2012) The flow field in turbulent round free jets. Prog Aerosp Sci 50:1–26

Bentley BJ, Leal LG (1986) An experimental investigation of drop deformation and breakup in steady, two-dimensional linear flows. J Fluid Mech 167(1):241

Bisten A, Schuchmann HP (2016) Optical measuring methods for the investigation of high-pressure homogenisation. Processes 4(41):1–19

Blonski S, Korczyk PM, Kowalewski TA (2007) Analysis of turbulence in a micro-channel emulsifier. Int J Therm Sci 46(11):1126–1141

Breuer MM (1985) Applications in the cosmetical industry. In: Becher P (ed) Encyclopedia of emulsion technology, volume 2: Applications. Marcel Dekker, Inc, New York

Brösel S, Schubert H (2001) Droplet disruption and coalescence in high-pressure homogenizers. In: Proceedings of the eighth international congress on engineering and food—ICEF, 8–1, pp 638–642

Budde C, Schaffner D, Walzel P (2002) Drop breakup in liquid-liquid dispersions at an orifice plate observed in a large-scale model. ChemEngTechnol 25(12):1164–1167

Cierpka C, Rossi M, Segura R, Mastrangelo F, Kähler CJ (2012) A comparative analysis of the uncertainty of astigmatism-mu PTV, stereo-mu PIV, and mu PIV. Exp Fluids 52(3):605–615

Danner T, Schubert H (2001) Coalescence processes in emulsions. In: Dickinson E, Miller R (eds), Food colloids: fundamentals of formulation, The Royal Society of Chemistry, London, pp 116–124

Davis SS, Hadgraft J, Palin KJ (1985) Medical and pharmaceutical applications of emulsions. In: Becher P (ed) Encyclopedia of emulsion technology, Volume 2: applications. Marcel Dekker, Inc, New York, pp 159–238

Floury J, Desrumaux A, LardiÞres J (2000) Effect of high-pressure homogenization on droplet size distributions and rheological properties of model oil-in-water emulsions. Innov Food Sci Emerg Technol 1(2):127–134

Gothsch T, Finke JH, Beinert S, Lesche C, Schur J, Buttgenbach S, Muller-Goymann C, Kwade A (2011) Effect of microchannel geometry on high-pressure dispersion and emulsification. ChemEngTechnol 34(3):335–343

Gothsch T, Schilcher C, Richter C, Beinert S, Dietzel A, Büttgenbach S, Kwade A (2014) High-pressure microfluidic systems (HPMS): flow and cavitation measurements in supported silicon microsystems. Microfluid Nanofluid 18(1):121–130

Gothsch T, Richter C, Beinert S, Schilcher C, Schilde C, Büttgenbach S, Kwade A (2016) Effect of cavitation on dispersion and emulsification process in high-pressure microsystems (HPMS). Chem Eng Sci 144:239–248

Grace HP (1982) Dispersion phenomena in high-viscosity immiscible fluid systems and application of static mixers as dispersion devices in such systems. Chem Eng Commun 14(3–6):225–277

Håkansson A, Fuchs L, Innings F, Revstedt J, Tragardh C, Bergenstahl B (2011) High resolution experimental measurement of turbulent flow field in a high pressure homogenizer model and its implications on turbulent drop fragmentation. ChemEngSci 66(8):1790–1801

Håkansson A, Innings F, Revstedt J, Trägårdh C, Bergenståhl B (2012) Estimation of turbulent fragmenting forces in a high-pressure homogenizer from computational fluid dynamics. Chem Eng Sci 75:309–317

Heusch R (1987) Emulsions. In: Gerhartz W, Ullmann F (eds) Ullmanns encyclopedia of industrial chemistry, 5th edn. VCH, Weinheim

Innings F, Tragardh C (2007) Analysis of the flow field in a high-pressure homogenizer. ExpThermFluid Sci 32(2):345–354

Kähler CJ, Scholz U, Ortmanns J (2006) Wall-shear-stress and near-wall turbulence measurements up to single pixel resolution by means of long-distance micro-PIV. Exp Fluids 41(2):327–341

Kähler CJ, Scharnowski S, Cierpka C (2012) On the resolution limit of digital particle image velocimetry. Exp Fluids 52(6):1629–1639

Karbstein H (1994) Untersuchungen zum Herstellen und Stabilisieren von Öl-in-Wasser-Emulsionen. Dissertation, Karlsruhe

Keane RD, Adrian RJ (1990) Optimization of particle image velocimeters. I. Double pulsed systems. Meas Sci Technol 1(11):1202–1215

Kelemen K, Crowther FE, Cierpka C, Hecht LL, Kähler CJ, Schuchmann HP (2014) Investigations on the characterization of laminar and transitional flow conditions after high pressure homogenization orifices. Microfluid Nanofluid 18(4):599–612

Kelemen K, Gepperth S, Koch R, Bauer H-J, Schuchmann HP (2015) On the visualization of droplet deformation and breakup during high-pressure homogenization. Microfluid Nanofluid 19(5):1139–1158

Kissling K, Schütz S, Piesche M (2011) Numerical investigation on the deformation of droplets in high-pressure homogenizers. In: Nagel WE, Kröner DB, Resch MM (eds) High performance computing in science and engineering '10. Springer, Stuttgart, pp 287–294

Köhler K, Schuchmann HP (2015) High-pressure homogenization with microstructured systems. In: Engineering aspects of food emulsification and homogenization. CRC Press, Boca Raton, pp 169–194

Kolb G, Wagner G, Ulrich J (2001) Untersuchungen zum Aufbruch von Einzeltropfen in Dispergiereinheiten zur Emulsionsherstellung. Chem Ing Tec 73:80–83

Koutsiaris AG, Mathioulakis DS, Tsangaris S (1999) Microscope PIV for velocity-field measurement of particle suspensions flowing inside glass capillaries. Meas Sci Technol 10(11):1037–1046

Lindken R, Rossi M, Grosse S, Westerweel J (2009) Micro-particle image velocimetry (microPIV): recent developments, applications, and guidelines. Lab A Chip 9(17):2551–2567

Massey BS, John W-S (1998) Mechanics of fluids. Crc Press

Meinhart CD, Wereley ST, Santiago JG (1999) PIV measurements of a microchannel flow. Exp Fluids 27(5):414–419

Merkel T, Hecht LL, Schoth A, Wagner C, Munoz-Espí R, Landfester K, Schuchmann HP (2015) Continuous preparation of polymer/inorganic composite nanoparticles via miniemulsion polymerization. In: Kind M, Peukert W, Rehage H, Schuchmann HP (eds) Colloid process engineering. Springer, Heildeberg, pp 345–370

Mielnik MM, Saetran LR (2004) Micro particle image velocimetry—an overview. Turbulence 10:83–90

Phipps LW (1975) The fragmentation of oil droplets in emulsions by a high-pressure homogenizer. JPhysD ApplPhys 8:448

Phipps LW (1982) Homogenizing valve design and its influence on milk fat globule dispersion II. High rate of flow. J Dairy Res 49:317–322

Plateau JAF (1873) Statique expérimentale et théorique des liquides soumis aux seules forces moléculaires. AcadSciBruxMem 2

Raffel M, Willert CE, Wereley ST, Kompenhans J (2007) Particle image velocimetry: a practical guide. Springer, Dordrecht

Ramamurthi K, Nandakumar K (1999) Characteristics of flow through small sharp-edged cylindrical orifices. Flow Meas Instrum 10(3):133–143

Reynolds O (1883) An experimental investigation of the circumstances which determine whether the motion of water shall be direct or sinuous, and of the law of resistance in parallel channels. Philos Trans R Soc Lond 174:935–982

Rossi M, Segura R, Cierpka C, Kähler CJ (2012) On the effect of particle image intensity and image preprocessing on the depth of correlation in micro-PIV. Exp Fluids 52(4):1063–1075

Rumscheidt FD, Mason SG (1961) Particle motions in sheared suspensions. XII. Deformation and burst of fluid drops in shear and hyperbolic flow. J Colloid Sci 16(3):238–261

Santiago JG, Wereley ST, Meinhart CD, Beebe DJ, Adrian RJ (1998) A particle image velocimetry system for microfluidics. Exp Fluids 25(4):316–319

Schlender M, Minke K, Schuchmann HP (2016) Sono-chemiluminescence (SCL) in a high-pressure double stage homogenization processes. Chem Eng Sci 142:1–11

Schuchmann HP (2016) Hydrodynamic pressure processing for enhancing emulsification and dispersion. In: Knoerzer K, Juliano P, Smithers GW (eds) Innovative food processing technologies: extraction, separation, component modification, and process intensification. Woodhead Publishing, Oxford

Stang M, Schuchmann HP, Schubert H (2001) Emulsification in high-pressure homogenizers. Eng Life Sci 1(4):151–157

Steiner H, Teppner R, Brenn G, Vankova N, Tcholakova S, Denkov N (2006) Numerical simulation and experimental study of emulsification in a narrow-gap homogenizer. ChemEngSci 61(17):5841–5855

Stone HA (1994) Dynamics of drop deformation and breakup in viscous fluids. Annu Rev Fluid Mech 26(1):65–102

Stone HA, Bentley BJ, Leal LG (1986) An experimental-study of transient effects in the breakup of viscous drops. J Fluid Mech 173:131–158

Taylor GI (1934) The formation of emulsions in definable fields of flow. Proc R Soc Lond Ser A 146(858):501–523

Tesch S, Schubert H (2001) Droplet deformation and disruption during the emulsification in a high-pressure homogenizer with an orifice valve. Chem Ing Tec 73(6):693

Tesch S, Freudig B, Schubert H (2002) Herstellen von Emulsionen in Hochdruckhomogenisatoren—Teil 1: Zerkleinern und Stabilisieren von Tropfen. Chem Ing Tec 74(6):875–880

Walstra P (1983) Formation of emulsions. In: Becher P (ed) Encyclopedia of emulsion technology, vol 1. Marcel Dekker Inc, New York, pp 57–128

Walstra P (1997) Making emulsions and foams: an overview. In: Dickinson E (ed) Food colloids: proteins, lipids and polysaccharides, papers pres. Ystad, Sweden on 24–26 April 1996, special publication/Royal society of chemistry; 192, Cambridge

Wereley ST, Meinhart CD (2010) Recent advances in micro-particle image velocimetry. Annu Rev Fluid Mech 42(1):557–576

Wibel W (2009) Untersuchungen zu laminarer, transitioneller und turbulenter Strömung in rechteckigen Mikrokanälen

Affiliations

Ariane Bisten[1] · **Dominik Rudolf[1]** · **Heike P. Karbstein[1]**

✉ Ariane Bisten
  ariane.bisten@kit.edu

[1] Institute of Process Engineering in Life Sciences, Section I: Food Process Engineering, Karlsruhe Institute of Technology, Kaiserstrasse 12, 76131 Karlsruhe, Germany